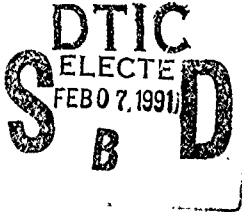


AD-A231 583

DTIC FILE COPY

REPORT DOCUMENTATION PAGE			Form Approved OMB No. 0704-0188	
Public reporting burden for this collection of information is estimated to average 1 hour per response, including the time for reviewing instructions, searching existing data sources, gathering and maintaining the data needed, and completing and reviewing the collection of information. Send comments regarding this burden estimate or any other aspect of this collection of information, including suggestions for reducing this burden, to Washington Headquarters Services, Directorate for Information Operations and Reports, 1215 Jefferson Davis Highway, Suite 1204, Arlington, VA 22202-4302, and to the Office of Management and Budget, Paperwork Reduction Project (0704-0188), Washington, DC 20503.				
1. AGENCY USE ONLY (Leave blank)	2. REPORT DATE 1990	3. REPORT TYPE AND DATES COVERED Thesis/DXXXXXXX		
4. TITLE AND SUBTITLE Application of the Finite Element Method to Random Rough Surface Scattering with Neumann Boundary Conditions		5. FUNDING NUMBERS		
6. AUTHOR(S) Kevin Krause				
7. PERFORMING ORGANIZATION NAME(S) AND ADDRESS(ES) AFIT Student at: University of Washington		8. PERFORMING ORGANIZATION REPORT NUMBER AFIT/CI/CIA - 90-136		
9. SPONSORING, MONITORING AGENCY NAME(S) AND ADDRESS(ES) AFIT/CI Wright-Patterson AFB OH 45433		10. SPONSORING/MONITORING AGENCY REPORT NUMBER		
11. SUPPLEMENTARY NOTES				
12a. DISTRIBUTION, AVAILABILITY STATEMENT Approved for Public Release IAW AFR 190-1 Distribution Unlimited ERNEST A. HAYGOOD, 1st Lt, USAF Executive Officer, Civilian Institution Programs		12b. DISTRIBUTION CODE		
13. ABSTRACT (Maximum 200 words)				
				
14. SUBJECT TERMS			15. NUMBER OF PAGES 50	
			16. PRICE CODE	
17. SECURITY CLASSIFICATION OF REPORT UNCLASSIFIED	18. SECURITY CLASSIFICATION OF THIS PAGE	19. SECURITY CLASSIFICATION OF ABSTRACT	20. LIMITATION OF ABSTRACT	

Application of the Finite Element Method
to Random Rough Surface Scattering
with Neumann Boundary Conditions

by

Kevin Krause

A thesis submitted in partial fulfillment
of the requirements for the degree of

Master of Science in Electrical Engineering

University of Washington

1990

Approved by

Long Tan
(Chairperson of Supervisory Committee)

Program Authorized
to Offer Degree

Elect. Eng.

Date

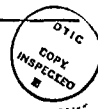
Nov. 26, 1990

91 2 06 094

In presenting this thesis in partial fulfillment of the requirements for a Master's degree at the University of Washington, I agree that the Library shall make its copies freely available for inspection. I further agree that extensive copying of this thesis is allowable only for scholarly purposes, consistent with "fair use" as prescribed in the U.S. Copyright Law. Any other reproduction for any purposes or by any means shall not be allowed without my written permission.

Signature Kevin C. Krause

Date 25 NOV 90



Accession For	
NTIS GRA&I	<input checked="checked" type="checkbox"/>
DTIC TAB	<input type="checkbox"/>
Unannounced	<input type="checkbox"/>
Justification	
By	
Distribution/	
Availability Codes	
Dist	Avail and/or Special
A-1	



University of Washington

Abstract

Application of the Finite Element Method
to Random Rough Surface Scattering
with Neumann Boundary Conditions

by Kevin Krause

Chairperson of Supervisory Committee:

Professor Leung Tsang

Department of Electrical Engineering

Antenna processing unit

Abstract:

Scattering from a one-dimensional rough surface with Gaussian roughness spectrum is analyzed using a finite element formulation. The method is applied to Monte Carlo simulations satisfying Neumann boundary conditions. Finite element results are compared with results obtained by solving an integral equation. Convergence of the method is verified by varying the number of nodal points in the first order, triangular mesh. Results are in excellent agreement with tapered wave integral equation solutions for large surface length after averaging over realizations. Finite element advantages in CPU time and memory storage are presented for the examples discussed. Comparisons with the Kirchoff approximation and small perturbation theory within their respective regions of validity are also presented. Additionally, analysis of the effects of decreasing surface length on incoherent scattering results of the finite element method is accomplished to investigate the method's likely advantages for large-scale scattering problems. Numerical Results of scattering are represented in terms of the normalized bistatic scattering cross section.

TABLE OF CONTENTS

List of Figures	iii
List of Tables	iv
Chapter 1 INTRODUCTION	1
Chapter 2 FINITE ELEMENT METHOD	3
2.1 Formulation	3
2.2 Implementation	8
2.3 Decomposition into Coherent and Incoherent Scattering	10
Chapter 3 PERTURBATION THEORY	13
3.1 Formulation	13
Chapter 4 KIRCHOFF APPROXIMATION	15
4.1 Formulation	15
Chapter 5 NUMERICAL RESULTS	17
5.1 Convergence of FEM with Respect to N_x and N_z	17
5.2 Comparison of FEM and TWIE for a Single Realization	18
5.3 Comparisons of CPU Time and Memory Storage	18
5.4 Comparison over 100 Realizations	19
5.5 Comparison of Power Conservation Tests	19
5.6 FEM Result Dependence on Surface Length	20
Chapter 6 CONCLUSIONS	41
Bibliography	42

LIST OF FIGURES

2.1	Problem Geometry	12
5.1	Convergence of FEM with Respect to N_x	22
5.2	Convergence of FEM with Respect to N_z	23
5.3	Comparison of FEM and TWIE for One Realization	24
5.4	Comparison of CPU Time for FEM and TWIE	25
5.5	Comparison of Memory Storage for FEM and TWIE	26
5.6	$\theta_i = 44.06^\circ$, $h/\lambda = 0.05$, $l/\lambda = 0.40$, $L/\lambda = 30.20$	27
5.7	Comparison of Nuemann and Dirichlet	28
5.8	$\theta_i = 0^\circ$, $h/\lambda = 0.10$, $l/\lambda = 1.00$, $L/\lambda = 70.50$	29
5.9	$\theta_i = 44.06^\circ$, $h/\lambda = 0.10$, $l/\lambda = 0.40$, $L/\lambda = 30.20$	30
5.10	$\theta_i = 44.06^\circ$, $h/\lambda = 0.20$, $l/\lambda = 0.40$, $L/\lambda = 30.20$	31
5.11	$\theta_i = 19.34^\circ$, $h/\lambda = 0.40$, $l/\lambda = 0.40$, $L/\lambda = 30.20$	32
5.12	Incoherent and Total Scattering Cross Sections	35
5.13	Comparison of FEM for $L/\lambda = 30.20$ and $L/\lambda = 24.45$	36
5.14	Comparison of FEM for $L/\lambda = 30.20$, and $L/\lambda = 20.13$	37
5.15	Comparison of FEM for $L/\lambda = 30.20$ and $L/\lambda = 14.38$	38
5.16	Comparison of FEM for $L/\lambda = 30.20$ and $L/\lambda = 10.07$	39
5.17	Comparison of FEM for $L/\lambda = 30.20$ and $L/\lambda = 4.31$	40

LIST OF TABLES

5.1	Percent Error Comparison Between FEM and TWIE	33
5.2	FEM Comparison for Different Surface Lengths	34

ACKNOWLEDGMENTS

I would like to express my sincere appreciation to the people who have helped me with this thesis. First, I would like to thank Mr. S.H. Lou for making his finite element computer code for Dirichlet boundary conditions and his rough surface generation routine available to me and for the numerous discussions and assistance that he provided in promoting my understanding of the problem. Without his assistance, it is likely that I wouldn't have finished on schedule. I wish to thank my advisor, Prof. Leung Tsang, for his guidance and support of my efforts throughout my work at the University of Washington. I would like to thank the additional members of my Master's committee: Prof. Chi Hou Chan, and Prof. Akira Ishimaru who have both been helpful and supportive of my efforts in research as well as in the classroom. Prof. Chan deserves additional thanks for helping me to locate a major problem in my finite element code. My thanks to Mr. Phillip Phu for his valuable assistance in the operation of the computer workstations. Finally, I would like to thank Mr. J.S. Chen for making his integral equation computer code available to me and for invaluable assistance in its use.

Chapter 1

INTRODUCTION

Scattering of electromagnetic waves from rough surfaces has been extensively studied using the Rayleigh-Rice perturbation theory and the Kirchoff approximation [2,6,16,17]. These classical approaches assume plane wave incidence upon arbitrarily long surfaces and utilize statistical properties in calculating ensemble averages. Each is, however, limited in its domain of validity which depends upon the surface characteristics.

With the advent of modern computers, increased interest in Monte Carlo simulations of scattering by random rough surfaces has evolved. In Monte Carlo simulations, ensemble averages are calculated by averaging scattered field intensity over hundreds of surface realizations. Computers are well suited for the task of averaging repetitive calculations, nonetheless, it is important to minimize the computation time for each realization.

The most common Monte Carlo method for an "exact" numerical result has been the solution of the tapered wave integral equation by the method of moments [1,3,5,16,17]. A plane wave is tapered to avoid edge effects from a finite surface using a Gaussian taper function which results in an incident wave consisting of an angular spectrum of plane waves about an average incident angle. Since the width of the angular spectrum is inversely proportional to surface length, large surface length is required to better approximate plane wave incidence. The disadvantage of the integral equation approach is that it requires solution of a full, complex matrix, and for large scale rough surface problems, applicability of the method is limited by available computer memory and CPU time.

In order to address these problems, application of the finite element method to Monte Carlo simulations of rough surface scattering has recently been investigated for one-dimensional Gaussian rough surfaces with periodic, Dirichlet boundary conditions [8,9]. In this thesis, existing finite element code for Dirichlet boundary conditions is converted and applied to Monte Carlo simulations of one-dimensional Gaussian rough

surfaces with periodic, Neumann boundary conditions. Accuracy of the results is verified by comparison with "exact" results determined through the use of a tapered wave integral equation (TWIE) solution with large surface length. Two propagating Floquet modes exist for each wavelength of surface length in the finite element approach. Since evanescent waves rapidly decay above the rough surface, a total number of only four to six evanescent modes are needed. In contrast, discretization in the integral equation approach requires ten points per wavelength. Hence, for a surface with $L/\lambda = 30$, the TWIE approach requires 300 basis functions while 66 modes are sufficient in the finite element approach [9]. Additionally, a full, complex matrix must be solved for the TWIE approach while a sparse, real matrix must be solved for the FEM approach. Thus, TWIE generally requires significantly more computer CPU time and memory storage. Surfaces are generated using Monte Carlo surface generation routines with Gaussian roughness spectrum and specified statistics. Additional comparisons with both the Rayleigh-Rice theory and the Kirchhoff approximation in their respective domains of validity are also made. Finally, tests are conducted to analyze the effects of decreasing surface length on incoherent scattering results of the finite element method. This is an important investigation since incoherent scattering is the measured quantity in monostatic and bistatic scattering, and analysis of smaller surface lengths requires much less CPU time and memory storage. The scattered field quantity calculated is the normalized bistatic scattering cross section.

Chapter 2

FINITE ELEMENT METHOD

In the finite element approach, scattering from an incident plane wave impinging upon a one-dimensional, random rough surface with Gaussian statistics is considered. Periodic boundary conditions are utilized to truncate the finite element mesh and to discretize the plane wave spectrum [2]. In the formulation, the scattered field in the region above the maximum height of the rough surface is expressed in terms of Floquet modes. The finite element method is utilized to solve the wave equation below the maximum height. The attraction of the finite element method is the banded nature of the resulting matrix equation and reduced memory storage requirements over those of the integral equation approach. Formulation of the finite element method is described in detail in reference [9] and will only be briefly summarized here.

2.1 Formulation

The geometry of scattering from a one-dimensional, periodic rough surface (two-dimensional scattering) in the xz plane is considered as illustrated in Figure 2.1. The surface has a Gaussian roughness spectrum, $W(K) = (h^2 l / 2\sqrt{\pi}) \exp(-K^2 l^2 / 4)$, and the random surface height is described by $z = f(x)$ with rms surface height h and correlation length l . The sample surface length L is extended periodically with period L in order that periodic boundary conditions may be used. A plane wave is incident on the surface with angle θ , from the vertical, and Neumann boundary conditions are imposed on the surface. Above the surface, the xz plane is divided into regions I and II, the homogeneous and inhomogeneous regions respectively. Region I consists of $z \geq d$ and region II consists of $d \geq z \geq f(x)$, with d chosen to be larger than the maximum height of the rough surface.

All field quantities are assumed to have $e^{-i\omega t}$ time dependence, and the incident field is a plane wave of the following form:

$$\psi_i(x, z) = e^{ik_{1x}x - ik_{1z}z} \quad (2.1)$$

where $k_{ix} = k \sin \theta_i$, $k_{iz} = k \cos \theta_i$, and $k = \omega \sqrt{\mu_0 \epsilon_0} = 2\pi/\lambda$. The incident field here differs from that used in the formulation of reference [9] by the factor $e^{-ik_{iz}d}$. This difference insures the same incident field for each realization despite variation in the parameter d —a necessary condition for the calculation of the incoherent scattering cross section. Use of periodic boundary conditions results in a discretization of the scattered plane wave spectrum into Floquet modes [7]. The scattered fields in region I consist of upward going waves only and can be expressed as:

$$\psi^I(x, z) = \sum_{m=-\infty}^{\infty} B_m e^{ik_{xm}x + ik_{zm}(z-d)} \quad (2.2)$$

with

$$k_{xm} = k_{ix} + \frac{2\pi m}{L}$$

$$k_{zm} = \begin{cases} \sqrt{k^2 - k_{xm}^2}, & k^2 - k_{xm}^2 \geq 0 \\ i\sqrt{k_{xm}^2 - k^2}, & k_{xm}^2 - k^2 > 0 \end{cases}$$

$m = 0, \pm 1, \pm 2, \dots$ Modal field amplitudes B_m are unknowns which are to be determined. From Floquet's theorem, $\psi_i(x + L, z) = e^{ik_{ix}L} \psi_i(x, z)$, and with discrete incident angle index m_0 , k_{ix} can be discretized by $k_{ix} = 2\pi m_0/L$ so that $\psi_i(x + L, z) = \psi_i(x, z)$. Incident angle can be any desired value since L/λ is a real number and not limited to an integer. Additionally, average scattered field intensity is independent of surface length as long as many correlation lengths are included. Truncating the Floquet expansion in equation (2.2) for the scattered field in region I and expressing it in Fourier series such that all propagating modes and $2N_E$ number of evanescent waves are included results in

$$\psi^I(x, z) = e^{i\frac{2\pi m_0}{L}x - ik_{iz}z} + \sum_{m=-N_E}^{N_E} B_{m-m_0} e^{i\frac{2\pi m}{L}x} e^{ik'_{zm}(z-d)} \quad (2.3)$$

with

$$k'_{zm} = \begin{cases} \sqrt{k^2 - \left(\frac{2\pi m}{L}\right)^2}, & k^2 - \left(\frac{2\pi m}{L}\right)^2 \geq 0 \\ i\sqrt{\left(\frac{2\pi m}{L}\right)^2 - k^2}, & \left(\frac{2\pi m}{L}\right)^2 - k^2 > 0 \end{cases}$$

where $N_3 = \text{int}(L/\lambda) + N_E$ and $\text{int}(L/\lambda)$ truncates L/λ to an integer. Writing equation (2.3) in the sine and cosine form of a Fourier series leads to

$$\begin{aligned} \psi^I(x, z) = & \cos \left[\frac{2\pi m_0}{L} x - k_{iz} z \right] + i \sin \left[\frac{2\pi m_0}{L} x - k_{iz} z \right] + a_0 e^{ik(z-d)} \\ & + \sum_{m=1}^{N_3} \left[a_m \cos \left(\frac{2\pi m}{L} x \right) + b_m \sin \left(\frac{2\pi m}{L} x \right) \right] e^{ik'_m(z-d)} \end{aligned} \quad (2.4)$$

For region II ($d \geq z \geq f(x)$), the finite element method is applied to determine the modal fields $\psi_m^{II}(x, z)$ where m is the modal index. Modal fields obey the following equations:

$$(\nabla^2 + k^2) \psi_m^{II,c}(x, z) = 0, \quad m = 0, 1, 2, \dots, N_3 \quad (2.5)$$

$$(\nabla^2 + k^2) \psi_m^{II,s}(x, z) = 0, \quad m = 1, 2, 3, \dots, N_3 \quad (2.6)$$

where superscripts c and s stand for cosine and sine respectively. Respective boundary conditions for each arc:

$$\frac{\partial \psi_m^{II,c}(x, f(x))}{\partial n} = 0 \quad (2.7)$$

$$\psi_m^{II,c}(-L/2, z) = \psi_m^{II,c}(L/2, z) \quad (2.8)$$

$$\psi_m^{II,c}(x, d) = \cos \left(\frac{2\pi m}{L} x \right) \quad (2.9)$$

$$\frac{\partial \psi_m^{II,s}(x, f(x))}{\partial n} = 0 \quad (2.10)$$

$$\psi_m^{II,s}(-L/2, z) = \psi_m^{II,s}(L/2, z) \quad (2.11)$$

$$\psi_m^{II,s}(x, d) = \sin \left(\frac{2\pi m}{L} x \right) \quad (2.12)$$

Equations (2.7) and (2.10) specify the Neumann boundary conditions and distinguish the work accomplished in this thesis from that of references [8] and [9].

The wave equations (2.5) and (2.6) along with equations (2.7)-(2.12) allow convenient solution for $\psi_m^{II,c}$ and $\psi_m^{II,s}$ by the finite element method for each modal index m . Discretization of region II is finite, and the modal field solutions are real, thus, only a real, sparse matrix solver is required [18].

After solving for the unknown modal fields, the total field in region II can be expressed as:

$$\psi^{II}(x, z) = F_0 \psi_0^{II,c}(x, z) + \sum_{m=1}^{N_3} [F_m \psi_m^{II,c}(x, z) + G_m \psi_m^{II,s}(x, z)] \quad (2.13)$$

allowing the real boundary conditions of equations (2.9) and (2.12) to be used.

The required number of equations to determine the unknown modal amplitudes B_m are obtained by matching the continuities of ψ^I and ψ^{II} and their normal derivatives at $z = d$. From equations (2.4) and (2.13) and the orthogonal properties of the sine and cosine functions, the following equations are obtained:

$$\delta_{mm_0} e^{-ik_{iz}d} + a_m = F_m, \quad m = 0, 1, \dots, N_3 \quad (2.14)$$

$$i\delta_{mm_0} e^{-ik_{iz}d} + b_m = G_m, \quad m = 1, 2, \dots, N_3 \quad (2.15)$$

$$\begin{aligned} -ik_{iz}\delta_{0m_0} e^{-ik_{iz}d} + ik_{z0} a_0 &= \frac{1}{L} \int_0^L dx F_0 \frac{\partial \psi_0^{II,c}}{\partial z}(x, d) \\ &+ \frac{1}{L} \sum_{M=1}^{N_3} \int_0^L dx \left[F_M \frac{\partial \psi_M^{II,c}}{\partial z}(x, d) + G_M \frac{\partial \psi_M^{II,s}}{\partial z}(x, d) \right] \end{aligned} \quad (2.16)$$

$$\begin{aligned} -ik_{iz}\delta_{mm_0} e^{-ik_{iz}d} + ik'_{zm} a_m &= \frac{2}{L} \int_0^L dx \cos\left(\frac{2\pi m}{L}x\right) F_0 \frac{\partial \psi_0^{II,c}}{\partial z}(x, d) \\ &+ \frac{2}{L} \sum_{M=1}^{N_3} \int_0^L dx \cos\left(\frac{2\pi m}{L}x\right) \\ &\times \left[F_M \frac{\partial \psi_M^{II,c}}{\partial z}(x, d) + G_M \frac{\partial \psi_M^{II,s}}{\partial z}(x, d) \right], \quad m \neq 0 \end{aligned} \quad (2.17)$$

$$\begin{aligned} k_{iz}\delta_{mm_0} e^{-ik_{iz}d} + ik'_{zm} b_m &= \frac{2}{L} \int_0^L dx \sin\left(\frac{2\pi m}{L}x\right) F_0 \frac{\partial \psi_0^{II,c}}{\partial z}(x, d) \\ &+ \frac{2}{L} \sum_{M=1}^{N_3} \int_0^L dx \sin\left(\frac{2\pi m}{L}x\right) \\ &\times \left[F_M \frac{\partial \psi_M^{II,c}}{\partial z}(x, d) + G_M \frac{\partial \psi_M^{II,s}}{\partial z}(x, d) \right], \quad m \neq 0 \end{aligned} \quad (2.18)$$

where δ_{mm_0} is the Kronecker delta. Substituting equations (2.14) and (2.15) into (2.16), (2.17), and (2.18) leads to the following equations in terms of the unknowns a_0 , a_m , and b_m .

$$\begin{aligned}
 & -i2ka_0 + a_0 \frac{2}{L} \int_0^L dx \frac{\partial \psi_0^{II,c}}{\partial z}(x, d) \\
 & + \sum_{M=1}^{N_2} \left\{ a_M \left[\frac{2}{L} \int_0^L dx \frac{\partial \psi_M^{II,c}}{\partial z}(x, d) \right] + b_M \left[\frac{2}{L} \int_0^L dx \frac{\partial \psi_M^{II,s}}{\partial z}(x, d) \right] \right\} \\
 & = e^{-ik_{iz}d} \left\{ -i2k_{iz}\delta_{0m_0} - \delta_{0m_0} \frac{2}{L} \int_0^L dx \frac{\partial \psi_0^{II,c}}{\partial z}(x, d) \right. \\
 & \quad \left. - \frac{2}{L} \int_0^L dx \frac{\partial \psi_{m_0}^{II,c}}{\partial z}(x, d) U_{m_0-1} - i \frac{2}{L} \int_0^L dx \frac{\partial \psi_{m_0}^{II,s}}{\partial z}(x, d) U_{m_0-1} \right\} \quad (2.19)
 \end{aligned}$$

$$\begin{aligned}
 & -ik'_{zm}a_m + a_0 \frac{2}{L} \int_0^L dx \cos\left(\frac{2\pi m}{L}x\right) \frac{\partial \psi_0^{II,c}}{\partial z}(x, d) \\
 & + \sum_{M=1}^{N_2} a_M \left[\frac{2}{L} \int_0^L dx \cos\left(\frac{2\pi m}{L}x\right) \frac{\partial \psi_M^{II,c}}{\partial z}(x, d) \right] \\
 & + b_M \left[\frac{2}{L} \int_0^L dx \cos\left(\frac{2\pi m}{L}x\right) \frac{\partial \psi_M^{II,s}}{\partial z}(x, d) \right] \\
 & = e^{-ik_{iz}d} \left\{ -ik_{iz}\delta_{mm_0} - \delta_{0m_0} \frac{2}{L} \int_0^L dx \cos\left(\frac{2\pi m}{L}x\right) \frac{\partial \psi_0^{II,c}}{\partial z}(x, d) \right. \\
 & \quad - \frac{2}{L} \int_0^L dx \cos\left(\frac{2\pi m}{L}x\right) \frac{\partial \psi_{m_0}^{II,c}}{\partial z}(x, d) U_{m_0-1} \\
 & \quad \left. - i \frac{2}{L} \int_0^L dx \cos\left(\frac{2\pi m}{L}x\right) \frac{\partial \psi_{m_0}^{II,s}}{\partial z}(x, d) U_{m_0-1} \right\}, \quad m \neq 0 \quad (2.20)
 \end{aligned}$$

$$\begin{aligned}
 & -ik'_{zm}b_m + a_0 \frac{2}{L} \int_0^L dx \sin\left(\frac{2\pi m}{L}x\right) \frac{\partial \psi_0^{II,c}}{\partial z}(x, d) \\
 & + \sum_{M=1}^{N_2} a_M \left[\frac{2}{L} \int_0^L dx \sin\left(\frac{2\pi m}{L}x\right) \frac{\partial \psi_M^{II,c}}{\partial z}(x, d) \right] \\
 & + b_M \left[\frac{2}{L} \int_0^L dx \sin\left(\frac{2\pi m}{L}x\right) \frac{\partial \psi_M^{II,s}}{\partial z}(x, d) \right] \\
 & = e^{-ik_{iz}d} \left\{ k_{iz}\delta_{mm_0} - \delta_{0m_0} \frac{2}{L} \int_0^L dx \sin\left(\frac{2\pi m}{L}x\right) \frac{\partial \psi_0^{II,c}}{\partial z}(x, d) \right. \\
 & \quad \left. + \frac{2}{L} \int_0^L dx \sin\left(\frac{2\pi m}{L}x\right) \frac{\partial \psi_{m_0}^{II,c}}{\partial z}(x, d) U_{m_0-1} \right. \\
 & \quad \left. + i \frac{2}{L} \int_0^L dx \sin\left(\frac{2\pi m}{L}x\right) \frac{\partial \psi_{m_0}^{II,s}}{\partial z}(x, d) U_{m_0-1} \right\}, \quad m \neq 0 \quad (2.21)
 \end{aligned}$$

$$\left. \begin{aligned} & -\frac{2}{L} \int_0^L dx \sin\left(\frac{2\pi m}{L}x\right) \frac{\partial \psi_{m_0}^{II,c}}{\partial z}(x,d) U_{m_0-1} \\ & -i\frac{2}{L} \int_0^L dx \sin\left(\frac{2\pi m}{L}x\right) \frac{\partial \psi_{m_0}^{II,s}}{\partial z}(x,d) U_{m_0-1} \end{aligned} \right\}, \quad m \neq 0$$

where $U_{m_0-1} = 0$ for normal incidence ($m_0 = 0$) and $U_{m_0-1} = 1$ for oblique incidence ($m_0 \neq 0$). In equations (2.19), (2.20), and (2.21), $\frac{\partial \psi_M^{II,c}}{\partial z}(x,d)$ and $\frac{\partial \psi_M^{II,s}}{\partial z}(x,d)$ are evaluated using an IMSL subroutine which takes the derivatives of quadratic interpolation of $\psi_M^{II,c}(x,z)$ and $\psi_M^{II,s}(x,z)$ along the z direction. Integrations are evaluated using Simpson's rule. After a_0 , a_m , and b_m are determined, the unknown modal field amplitudes, B_m , can be determined by the following:

$$B_{-m_0} = a_0 \quad (2.22)$$

$$B_{m-m_0} = \frac{1}{2}(a_m - ib_m), \quad N_3 \geq m > 0 \quad (2.23)$$

$$B_{-m-m_0} = \frac{1}{2}(a_m + ib_m), \quad N_3 \geq m > 0 \quad (2.24)$$

2.2 Implementation

Neumann boundary conditions are a natural result of the Galerkin procedure applied to the finite element method here. In the finite element implementation, three general factors affect the accuracy of the solution: (i) N_x , the number of nodes along the x -axis, (ii) N_z , the number of nodes along the z -axis, and (iii) $2N_E$, the number of evanescent modes considered. The parameter d must be set to be above the maximum height of the rough surface allowing some variation of the field from its surface value to its value at $z = d$, yet small enough to minimize the number nodes in the z direction. Convergence of the method is verified by increasing N_x , N_z , and $2N_E$. As it turns out, the number of evanescent modes is not a sensitive parameter relative to power-conservation tests [9]. For the numerical examples examined with the finite element method, the following parameter values are used, $2N_E = 4$, $N_x/\lambda \approx 10$ and $N_z/l \approx 7$ for $l = 0.4\lambda$ and $N_x/\lambda \approx 10$ for $l = \lambda$. The parameter d is set at 0.1λ above the maximum surface height for each realization.

Following standard finite element procedure, region II is divided into a number of first-order, triangular elements. The modal field for each mode m within each

element (e) is expressed in terms of the field at the three nodes of each triangle in the following matrix notation:

$$\psi_m^{(e)}(x, z) = [N^{(e)}] \{ \psi^{(e)} \} \quad (2.25)$$

Field values at the three nodes are represented by $\psi^{(e)}$, $[N^{(e)}]$ are linear interpolation functions for each element (e), and $\{ \cdot \}$ and $[\cdot]$ denote a column and row vector respectively. Complete representation of the modal field in region II consisting of M elements follows:

$$\psi_m^{II}(x, z) = \sum_{e=1}^M \psi_m^{(e)}(x, z) = \sum_{e=1}^M [N^{(e)}] \{ \psi^{(e)} \} \quad (2.26)$$

After substituting equation (2.26) into equations (2.5) and (2.6) and applying the Galerkin procedure, the following results:

$$[A] \{ \psi \} = \{ P \} \quad (2.27)$$

where

$$[A] = \sum_{e=1}^M \left[\int \int_e \left\{ \frac{\partial N^{(e)}}{\partial x} \right\} \left[\frac{\partial N^{(e)}}{\partial x} \right] + \left\{ \frac{\partial N^{(e)}}{\partial z} \right\} \left[\frac{\partial N^{(e)}}{\partial z} \right] dx dz \right. \\ \left. - k^2 \int \int_e \{ N^{(e)} \} [N^{(e)}] dx dz \right]$$

Region II has a total of $N_x N_z$ free and prescribed nodes and $2(N_x - 1)(N_z - 1)$ number of elements. There are N_x number of prescribed nodes at the boundary $z = d$. Neumann boundary conditions are a natural result of the Galerkin procedure. Hence, surface nodes are considered free nodes and surface node field values are determined in the same manner as nodal field values in the interior of region II. For periodic boundary conditions at x and $x + L$, field values must be identical but their values are unknown. The periodicity is satisfied by setting the global node numbers at x and $x + L$ to the same value for a fixed z . As a result, ψ in (2.29) is a $(N_x - 1)(N_z - 1)$ column vector of free nodes only, $[A]$ is a $(N_x - 1)(N_z - 1)$ by $(N_x - 1)(N_z - 1)$ real and symmetric matrix with half-bandwidth $2N_z$ corresponding to the global assembly of free nodes. P is a $(N_x - 1)(N_z - 1)$ column vector of assembled prescribed nodes.

Equation (2.27) must be solved once for each of the $(2N_3 + 1)$ modes in (2.5) and (2.6). A direct sparse matrix solver utilizing LU decomposition and backsubstitution is used [18]. Since $[A]$ is sparse and symmetric, profile storage of its upper half only significantly reduces memory storage requirements. The square matrix $[A]$ contains only free nodes and remains unchanged for all of the modes, hence, the matrix solver accomplishes LU decomposition once and backsubstitution $(2N_3 + 1)$ times.

Results of the TWIE method are computed in terms of the bistatic scattering cross section as defined in [16]. For convenience, TWIE results are plotted using a normalized cross section $\sigma(\theta_s)/\cos\theta_i$ so that the integral over all scattered angles θ_s reduces to unity for power conservation. In the discrete case of the finite element method, the sum of scattered power over all discrete scattered angles θ_m must reduce to unity. Since $\sum_m |B_m|^2 \cos\theta_m / \cos\theta_i = \int d\theta_m L \cos\theta_m |B_m|^2 \cos\theta_m / \cos\theta_i$, the normalized bistatic scattering cross section for all discrete scattered angles is defined as $L|B_m|^2 \cos^2\theta_m / \cos\theta_i$.

2.3 Decomposition into Coherent and Incoherent Scattering

Analysis of the effects of decreasing surface length on finite element results over 100 realizations is accomplished by plotting the incoherent scattering cross section. This is an important result since it is the measured quantity in monostatic and bistatic scattering. The incoherent scattering cross section is calculated by first determining the incoherent intensity as defined in the following:

$$\langle |\psi_m|^2 \rangle - |\langle \psi_m \rangle|^2 \quad (2.28)$$

where

$$\psi_m = B_m e^{ik_{xm}z + ik_{ym}(z-d)} \quad (2.29)$$

$\langle |\psi_m|^2 \rangle$ is the total scattered intensity, $|\langle \psi_m \rangle|^2$ is the coherent scattered intensity, and $m = 0, \pm 1, \pm 2, \dots$. Since the parameter d varies with each surface realization depending upon its respective maximum height, the $e^{ik_{ym}(z-d)}$ phase term must be considered in the incoherent scattering cross section calculation. Therefore, after the modal scattered fields B_m are determined for each surface realization, their corresponding ψ_m values are determined at $z = d_{max}$. The value for d_{max} is defined

as the maximum d value for all 100 realizations. Hence, each field value and the subsequent incoherent scattering cross section calculation is referenced to a common phase point at the maximum d .

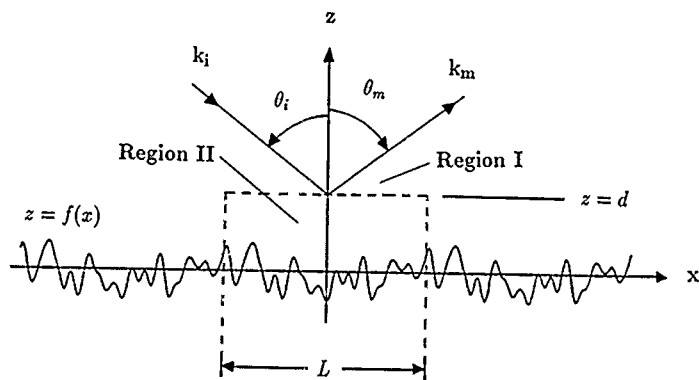


Figure 2.1: Problem Geometry

Chapter 3

PERTURBATION THEORY

The Rayleigh-Rice small perturbation theory (SP) is typically thought to be valid for slightly rough surfaces. More specifically, the rms surface height h should be small compared to wavelength of the incident field. This is usually expressed as $kh \ll 1$ with k being the wavenumber [17]. A recent study by Thorsos in reference [17] better clarifies the limits of validity of the first order perturbation theory which is used here for comparison with the finite element method.

3.1 Formulation

In the classical approach to the perturbation theory, the scattered field is represented as a superposition of outgoing plane waves [17]. The scattered intensity is averaged using the statistical properties of the rough surfaces. Considering plane wave incidence and expressing the scattered field as a superposition of plane waves, the following expression for the scattered field in the region above the rough surface results:

$$\psi_s = \sum_{m=-\infty}^{\infty} B_m e^{ik_{xz}z + ik_{mx}} \quad (3.1)$$

The unknown scattered plane wave amplitudes are represented by B_m . Applying Neumann boundary conditions on the surface, expanding in smallness, and averaging according to statistical theory, the following expression results for the average scattered intensity:

$$\langle |\psi_{sm}|^2 \rangle = \delta_{mm_0} + 4 \frac{[k_{iz}^2 - k_{sz}k_{ix} - k_{ix}^2]^2 h^2 l \sqrt{\pi}}{k_{sz}^2 L} e^{-\frac{z^2}{L}} \quad (3.2)$$

where

$$k_{ix} = \frac{2\pi m_0}{L}$$

$$\begin{aligned}
 k_{iz} &= \sqrt{k^2 - k_{ix}^2} \\
 p &= k_{sz} - k_{iz} \\
 k_{sx} &= \frac{2\pi m}{L} \\
 k_{sz} &= \sqrt{k^2 - k_{sx}^2}
 \end{aligned}$$

L is the surface length, h is the rms surface height, l is the correlation length, and m_0 is the discrete incident angle index as in the finite element analysis. Both the coherent and incoherent contributions to the average scattered intensity are included in equation (3.2) with the Kronecker delta function representing the coherent component. The one-dimensional equivalent to the normalized bistatic scattering cross section required for comparison with finite element results follows from the average scattered intensity:

$$\sigma(\theta_m) = \frac{L \cos^2 \theta_m}{\cos \theta_i} \left\{ \delta_{mm_0} + 4 \frac{[k_{iz}^2 - k_{sx} k_{iz} - k_{iz}^2]^2}{k_s^2} \frac{h^2 l \sqrt{\pi}}{L} e^{-\frac{p^2 l^2}{4}} \right\} \quad (3.3)$$

Perturbation results are presented in terms of discrete scattered angles in an identical manner to the finite element method.

Chapter 4

KIRCHOFF APPROXIMATION

The Kirchhoff approximation (KA) is generally thought to apply to gently undulating surfaces which are defined as surfaces with a radius of curvature that is large compared to a wavelength. This criterion places no general restrictions upon the surface height, and the Kirchhoff approximation has been applied to higher frequency cases than the perturbation theory as a result. Recent investigations by Thorsos better quantify the domain of validity for the Kirchhoff approximation as presented in reference [16].

4.1 Formulation

The classical starting point for the Kirchhoff approximation is the Helmholtz integral which defines the scattered field in relation to the surface field as presented in the following:

$$\psi(\mathbf{r}) = \int_s ds' \left[\psi(\mathbf{r}') \frac{\partial G_0(\mathbf{r}, \mathbf{r}')}{\partial n'} - G_0(\mathbf{r}, \mathbf{r}') \frac{\partial \psi(\mathbf{r}')}{\partial n'} \right] \quad (4.1)$$

The following substitutions are made for the appropriate far field Green's function, Neumann boundary conditions, and assumed plane wave incidence:

$$G_0 \approx \frac{1}{4} H_0^{(1)}(k|\mathbf{r} - \mathbf{r}'|) \approx \frac{1}{4} \left(\frac{2}{\pi k} \right)^{\frac{1}{2}} e^{-i\frac{\pi}{4}} \frac{e^{ikR}}{\sqrt{R}} e^{-ik_s \cdot \mathbf{r}'} \quad (4.2)$$

$$\frac{\partial \psi(\mathbf{r}')}{\partial n'} = 0 \quad (4.3)$$

$$\psi(\mathbf{r}') = 2\psi_i(\mathbf{r}') \quad (4.4)$$

$$\psi_i(\mathbf{r}') = e^{ik_{1,x}x' - ik_{1,z}f(x')} = e^{ik_1 \cdot \mathbf{r}'} \quad (4.5)$$

Theoretical averaging of the scattered intensity is accomplished using the statistical properties of the rough surface as in the perturbation theory. Combining the coherent

and incoherent contributions to the normalized bistatic scattering cross section, the following results:

$$\sigma(\theta_m) = \frac{1}{2\pi k} e^{-v_z^2 h^2} \left(\frac{\mathbf{v} \cdot \mathbf{k}_s}{v_z} \right)^2 \left[\frac{4 \sin^2 \left(\frac{v_z L}{2} \right)}{L v_z^2} + \sqrt{\pi} i \sum_{n=1}^{\infty} \frac{(v_z h)^{2n}}{n! \sqrt{n}} e^{-\frac{v_z^2 L^2}{4n}} \right] \quad (4.6)$$

where

$$\begin{aligned} k_{iz} &= \frac{2\pi m_0}{L} \\ \mathbf{v} &= k(\sin \theta_i - \sin \theta_m) \hat{\mathbf{x}} - k(\cos \theta_i + \cos \theta_m) \hat{\mathbf{z}} \\ \mathbf{k}_s &= k \sin \theta_m \hat{\mathbf{x}} + k \cos \theta_m \hat{\mathbf{z}} \\ v_x &= k(\sin \theta_i - \sin \theta_m) \\ v_z &= k(\cos \theta_i + \cos \theta_m) \end{aligned}$$

Results are presented in terms of discrete scattered angles in an identical manner to the finite element method.

Chapter 5

NUMERICAL RESULTS

Numerical results and comparisons of FEM, TWIE, SP, and KA are presented in this chapter. Section 5.1 provides convergence test results for FEM with respect to the number of nodes in both the x and z directions. Section 5.2 compares the FEM and TWIE result for the analysis of a single surface realization. Comparisons between FEM and TWIE with respect to required computer CPU time and memory storage are presented in section 5.3. Section 5.4 presents a comparison of each of the four approaches for various surface characteristics. Power conservation test results are compared for FEM and TWIE in section 5.5. Finally, section 5.6 presents an analysis of the effects of decreasing surface length on FEM results.

For each FEM and TWIE result in sections 5.4, 5.5, and 5.6, 100 surface realizations are generated with predetermined rms surface height, h/λ , correlation length, l/λ , and surface length, L/λ . The rms surface slope s , rms height, correlation length, and rms slope angle γ are related by $s = \sqrt{2}h/l = \tan \gamma$. The FEM and TWIE programs are then executed in order to calculate the ensemble average over the realizations. In the TWIE method, the incident wave consists of a plane wave which is tapered using a Gaussian taper function. The result is an incident wave consisting of an angular spectrum of plane waves about the incident angle with a width of approximately $4\lambda/(\sqrt{2\pi}L \cos \theta_i)$ [16]. TWIE results presented in this thesis are based on the computer code of reference [4].

5.1 Convergence of FEM with Respect to N_x and N_z

Figure 5.1 illustrates the effect on the finite element result of increasing the number of nodes in the x direction from $N_x = 301$ to $N_x = 601$ for a single realization with $\theta_i = 0^\circ$, $h/\lambda = 0.1$, $l/\lambda = 1.0$, and $L/\lambda = 30.2$. Figure 5.2 illustrates the effect of increasing the number of nodes in the z direction from $N_z = 8$ to $N_z = 15$ for the same realization. In each case, there is virtually no noticeable difference between the

respective dB plots. Hence, these two plots demonstrate convergence of the FEM result with respect to the number of nodes in both the x and z directions.

5.2 Comparison of FEM and TWIE for a Single Realization

Figure 5.3 compares the result of FEM and TWIE analysis of the same surface realization used to test FEM convergence with respect to increasing N_x and N_z . It is evident that differences do exist between the two methods for a single realization. This is to be expected as the FEM and TWIE approaches effectively see two different realizations since the former has periodic boundary conditions and the latter utilizes a tapered incident wave. With surface length $L/\lambda = 30.2$, the incident wave has an angular width of about $\pm 1.5^\circ$ with $\theta_i = 0^\circ$ for TWIE. Despite differences between FEM and TWIE for a single realization, results are excellent upon averaging over many realizations as illustrated in section 5.4.

5.3 Comparisons of CPU Time and Memory Storage

In Figures 5.4 and 5.5, CPU time and memory storage requirements for FEM and TWIE approaches are compared. Results are based upon the use of a VAX Station 3500 for a single realization with $h/\lambda = 0.1$ and $l/\lambda = 0.4$. Plots are made as a function of surface length with CPU time presented in seconds and memory storage presented in Megabytes. It is evident from the plots that TWIE generally requires more CPU time and memory storage than FEM. This is true when considering scattering problems where dimensions of the scattering geometry are much greater in one direction than in the other. Scattering from a one-dimensional surface with large surface length meets this criterion, hence, the sparsity of the real FEM matrix for solving equation (2.27) results in significant savings in CPU time and memory storage as compared to TWIE which requires full, complex matrix solution and storage. The disparity between the two methods becomes more significant as surface length increases, and it should be noted that a large surface length is required in the TWIE approach in order to minimize the angular spectrum of the incident field and more accurately predict the scattering cross section.

5.4 Comparison over 100 Realizations

Figure 5.6 compares the analytical perturbation theory to the FEM and TWIE results averaged over 100 surface realizations with $\theta_i = 44.06^\circ$ ($m_0 = 21$), $h/\lambda = 0.05$, $l/\lambda = 0.4$, and $L/\lambda = 30.2$. Surface characteristics are in the domain of validity of the small perturbation theory, and results agree well with FEM and TWIE results. A comparison between the small perturbation theory and FEM for Neumann and Dirichlet boundary conditions is presented in Figure 5.7. Dirichlet results are based on the finite element code of reference [9]. Surface characteristics are the same as in the previous illustration. Neumann boundary conditions result in a more diffuse scattered field than that of the Dirichlet as is evident in Figure 5.7. Results in Figure 5.8 compare the Kirchhoff approximation to FEM and TWIE. Surface realizations are such that $\theta_i = 0^\circ$ ($m_0 = 0$), $h/\lambda = 0.1$, $l/\lambda = 1.0$, and $L/\lambda = 70.5$. The Kirchhoff approximation is considered valid in this case, and results are excellent except for scattered grazing angles beyond $\pm 50^\circ$ where KA underpredicts the scattered intensity. Figure 5.9 illustrates the effect of increasing the rms slope angle γ which becomes 19.47° as compared to 8.05° in Figure 5.8. As expected, the angular distribution of the incoherent component to scattering cross section is increased. With $\theta_i = 44.06^\circ$ ($m_0 = 21$), $h/\lambda = 0.1$, $l/\lambda = 0.4$, and $L/\lambda = 30.2$, KA results are excellent for $\theta_s > 20^\circ$, but KA significantly underpredicts scattered intensity for $\theta_s < 20^\circ$. In Figure 5.10, h/λ has been increased from 0.1 to 0.2. As expected, the coherent component (specular peak) is significantly reduced from that of Figure 5.9. The KA results are generally poor except for $10^\circ \leq \theta_s \leq 47^\circ$ although improvement over Figure 5.9 is evident for $\theta_s < 0^\circ$. The rms height h/λ is increased to 0.4 in Figure 5.11 which results in $\gamma = 54.74^\circ$. KA is no longer valid, hence, only FEM and TWIE results are presented. As in all previous plots averaged over 100 realizations, agreement between TWIE and FEM is excellent. The specular peak has completely subsided in Figure 5.11 which is not surprising given the rather large rms height specified.

5.5 Comparison of Power Conservation Tests

Table 5.1 compares power conservation results of FEM and TWIE for Figure 5.6 and Figures 5.8-5.10. Negative values indicate an overprediction of scattered power, while

positive values indicate an underprediction. In general, FEM has less error in terms of power conservation than TWIE with the largest value being only -7.9×10^{-3} percent.

5.6 FEM Result Dependence on Surface Length

In order to investigate the effects of decreasing surface length on FEM results, further tests with 100 surface realizations are conducted. The coherent component to the scattering cross section is subtracted to avoid plotting a specular peak which broadens with decreasing surface length. Incoherent intensity, $\langle |\psi_m|^2 \rangle - |\langle \psi_m \rangle|^2$, is calculated at the maximum d for all 100 surface realizations. Surface realization characteristics $h/\lambda = 0.141$ and $l = 0.4$ for all surface lengths are chosen to produce a relatively high rms slope of $s = 0.5$. High rms slope for the realizations insures a broad angular distribution of the incoherent result. Figure 5.12 illustrates the removal of the coherent contribution to the total scattering cross section for $L/\lambda = 30.2$. A depression in the incoherent scattering cross section at $\theta_m = \theta_i$ results after removing the specular peak. This occurrence is unexplained by scattering theory, and more work is required to determine why it exists. The incoherent result of Figure 5.12 is plotted against results of all other surface lengths tested. Surface length is decreased in approximately 5λ intervals from $L/\lambda = 30.2$. Actual surface length values are arrived at through consideration of integer values for m_0 in order that $\theta_i \approx 44.06^\circ$ for all surfaces tested. Table 5.2 displays the specific criteria chosen for each test. Figures 5.13-5.17 compare the incoherent result for respective surface lengths of 24.45λ , 20.13λ , 14.38λ , 10.07λ , and 4.31λ . An IMSL subroutine is used to interpolate points for $L/\lambda \leq 14.38$. Excellent agreement can be seen between results down to $L/\lambda = 10.07$. Results for $L/\lambda = 4.31$ are also excellent for $\theta_m \leq 30^\circ$. However, due to the limited number of scattered angles for which scattering cross section values are calculated, the dip at $\theta_m = \theta_i$ has a significant effect. Table 5.2 also compares required computer storage and CPU time for each test. Memory storage is presented in megabytes for a single realization, and CPU time is presented in seconds for the full 100 realizations on a VAX 6000-440 workstation. Significant savings between $L/\lambda = 30.2$ and $L/\lambda = 10.07$ in storage and CPU time is evident. Test results are encouraging for eventual FEM analysis of two-dimensional surface scattering.

Since the surface length required for accurate FEM results is relatively small, it is possible that CPU time and memory storage could be kept within reasonable limits.

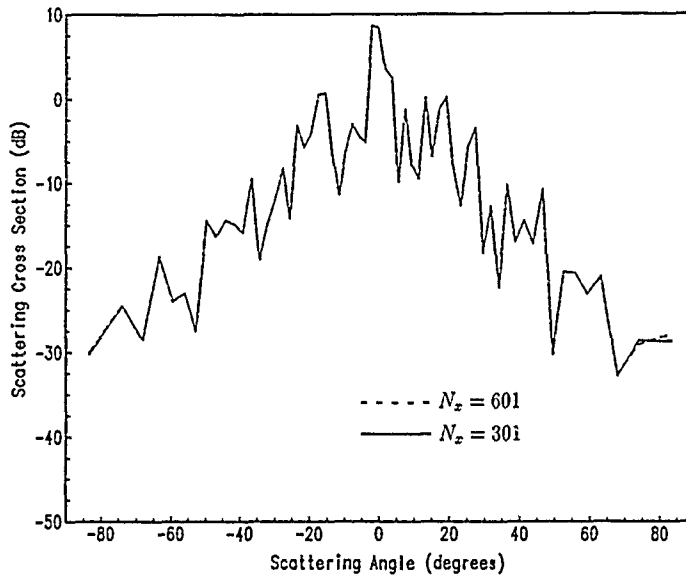


Figure 5.1: Convergence of FEM with Respect to N_x : ($\theta_s = 0^\circ$, $h/\lambda = 0.10$, $l/\lambda = 1.00$, $L/\lambda = 30.20$)

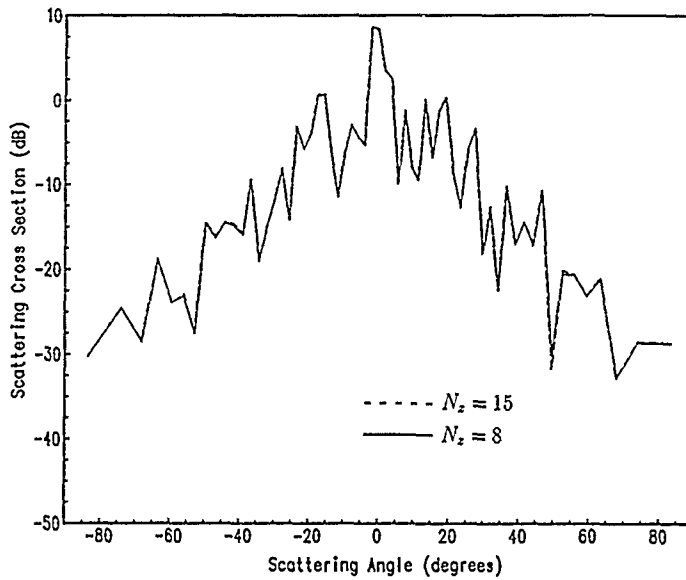


Figure 5.2: Convergence of FEM with Respect to N_z : ($\theta_i = 0^\circ$, $h/\lambda = 0.10$, $l/\lambda = 1.00$, $L/\lambda = 30.20$)

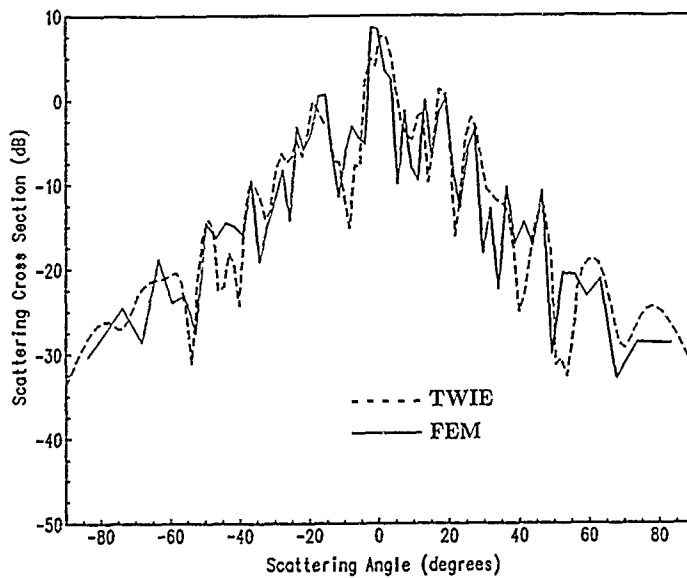


Figure 5.3: Comparison of FEM and TWIE Results for One Realization: ($\theta_i = 0^\circ$, $h/\lambda = 0.10$, $l/\lambda = 1.00$, $L/\lambda = 30.2$)

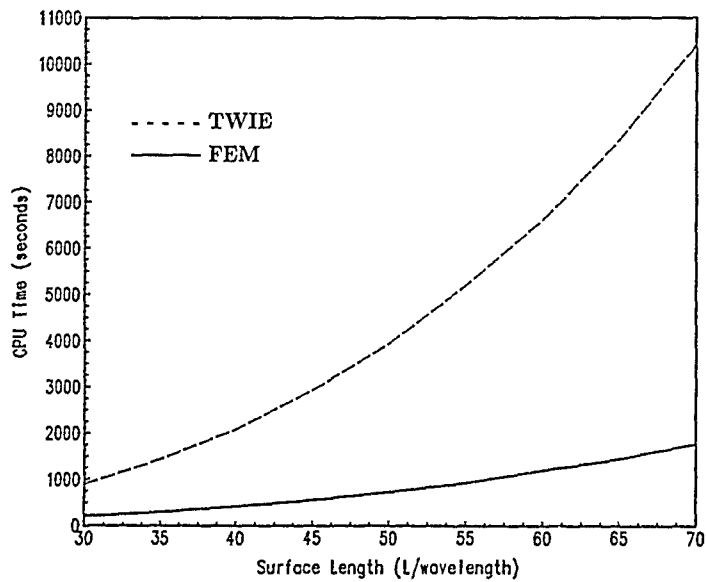


Figure 5.4: Comparison of CPU Time for FEM and TWIE: ($h/\lambda = 0.10$, $l/\lambda = 0.40$)

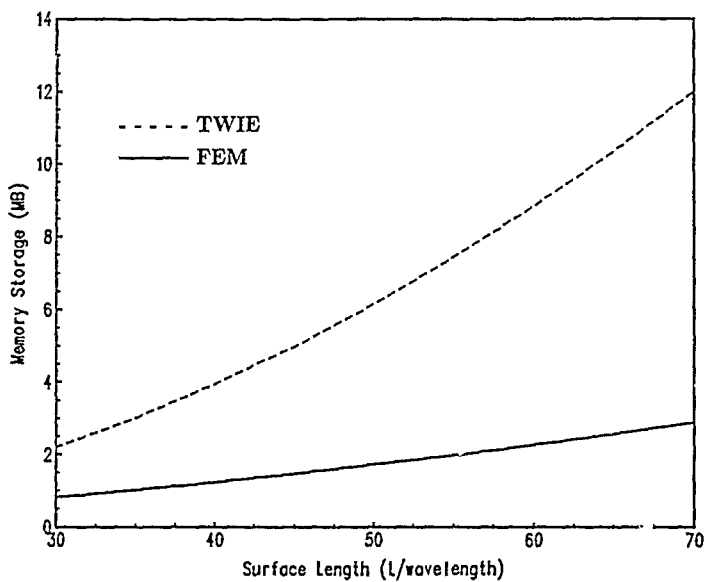


Figure 5.5: Comparison of Memory Storage for FEM and TWIE: ($h/\lambda = 0.10$, $l/\lambda = 0.40$)

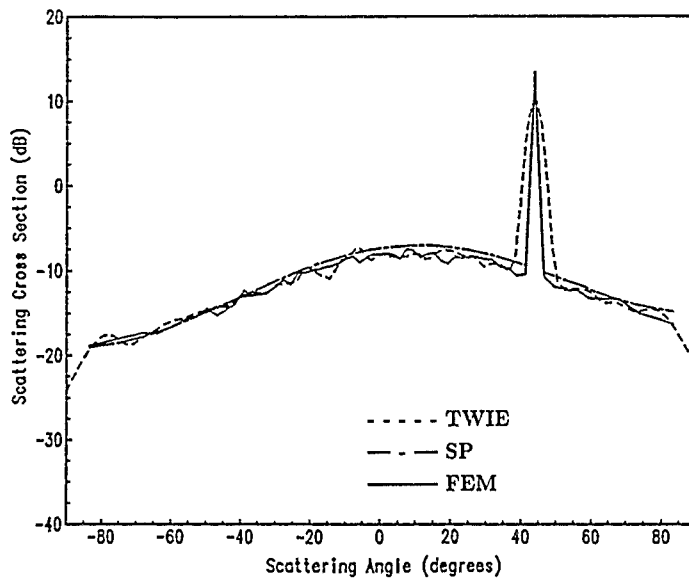


Figure 5.6: Comparison of SP, FEM, and TWIE: ($\theta_i = 44.06^\circ$, $h/\lambda = 0.05$, $l/\lambda = 0.40$, $L/\lambda = 30.20$)

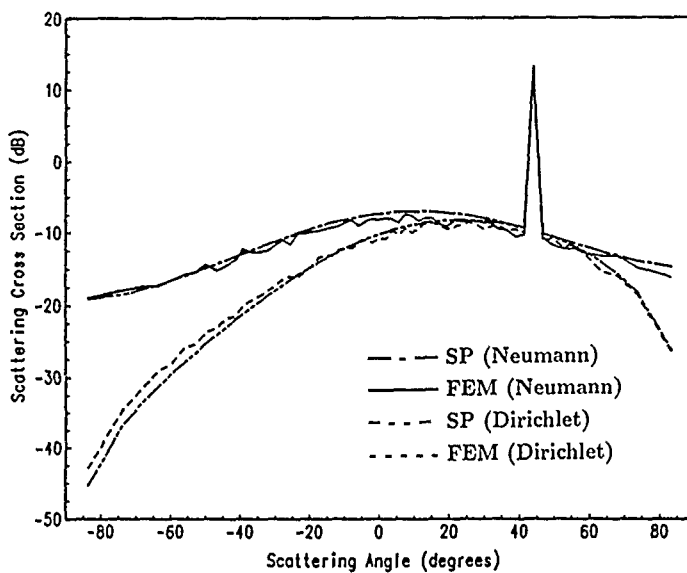


Figure 5.7: Comparison of SP and FEM for Neumann and Dirichlet Boundary Conditions: ($\theta_i = 44.06^\circ$, $h/\lambda = 0.05$, $l/\lambda = 0.40$, $L/\lambda = 30.20$)

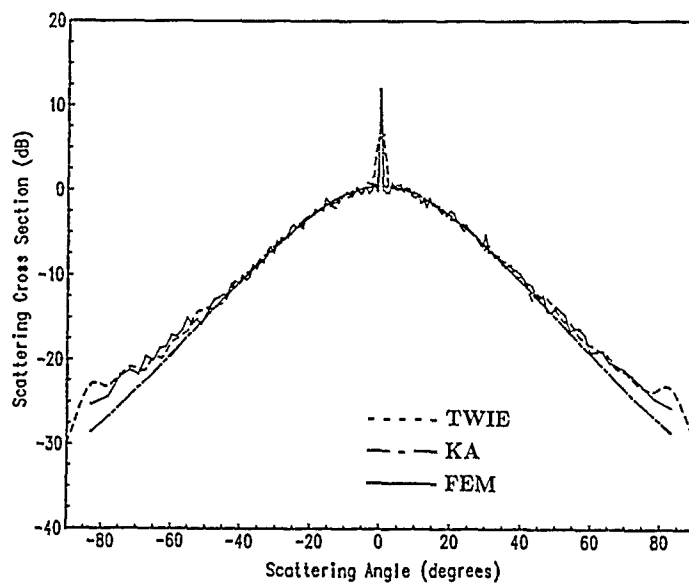


Figure 5.8: Comparison of KA, FEM, and TWIE: ($\theta_i = 0^\circ$, $h/\lambda = 0.10$, $l/\lambda = 1.00$, $L/\lambda = 70.50$)

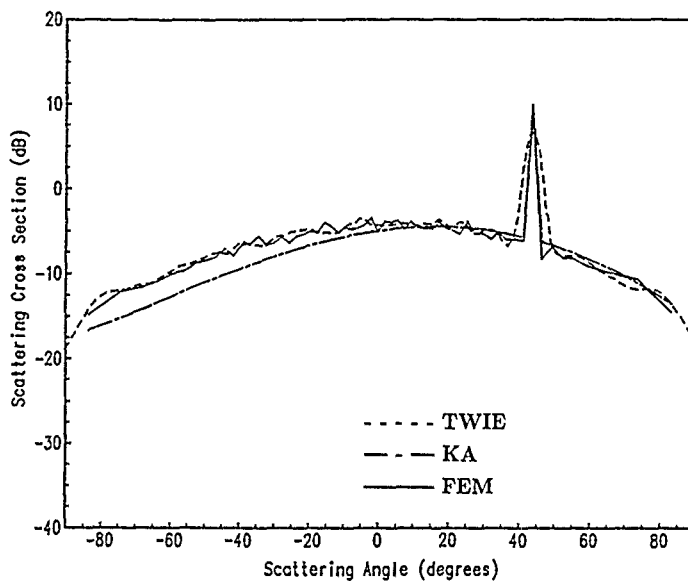


Figure 5.9: Comparison of KA, FEM, and TWIE: ($\theta_i = 44.06^\circ$, $h/\lambda = 0.10$, $l/\lambda = 0.40$, $L/\lambda = 30.20$)

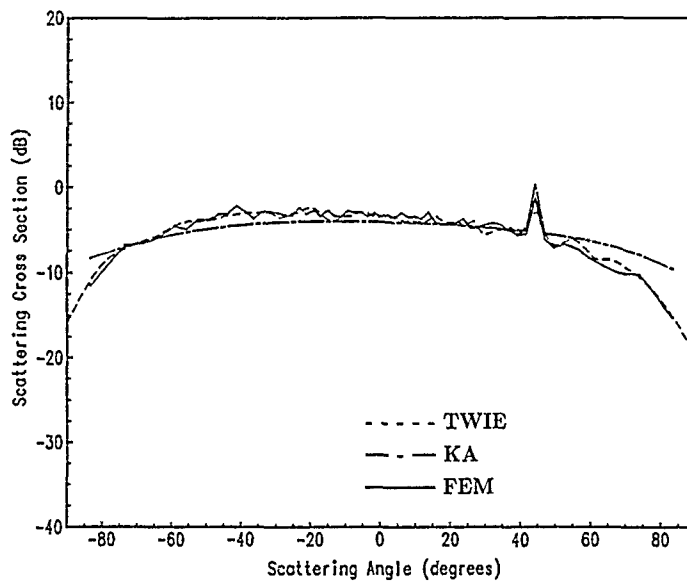


Figure 5.10: Comparison of KA, FEM, and TWIE: ($\theta_i = 44.06^\circ$, $h/\lambda = 0.20$, $l/\lambda = 0.40$, $L/\lambda = 30.20$)

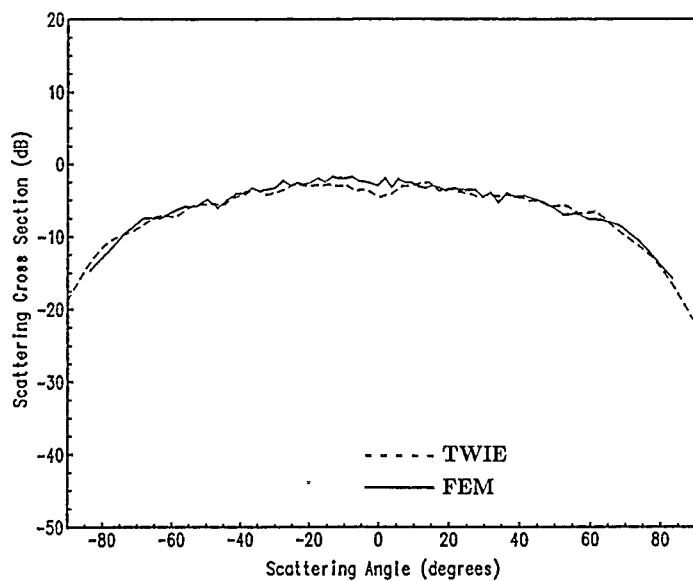


Figure 5.11: Comparison of FEM and TWIE: ($\theta_c = 19.34^\circ$, $h/\lambda = 0.40$, $l/\lambda = 0.40$, $L/\lambda = 30.20$)

Table 5.1: Percent Error Comparison Between FEM and TWIE

Figure #	h/λ	l/λ	L/λ	N_x	N_z	FEM	TWIE
5.6	0.05	0.40	30.20	525	8	$-2.2 \times 10^{-3}\%$	0.3%
5.8	0.10	1.00	70.50	705	8	$4.7 \times 10^{-4}\%$	3.8%
5.9	0.10	0.40	30.20	525	8	$-7.9 \times 10^{-3}\%$	1.1%
5.10	0.20	0.40	30.20	525	15	$2.9 \times 10^{-3}\%$	2.6%

Table 5.2: FEM Comparison for Different Surface Lengths

Figure #	L/λ	m_0	θ_i	N_x	N_z	Memory (MB)	CPU Time (sec)
5.12	30.20	21	44.06°	525	13	1.41	1.108×10^4
5.13	24.45	17	44.05°	427	13	1.09	6.750×10^3
5.14	20.13	14	44.07°	351	13	0.87	4.482×10^3
5.15	14.38	10	44.06°	251	13	0.59	2.326×10^3
5.16	10.07	7	44.04°	175	13	0.40	1.285×10^3
5.17	4.31	3	44.11°	75	13	0.16	3.561×10^2

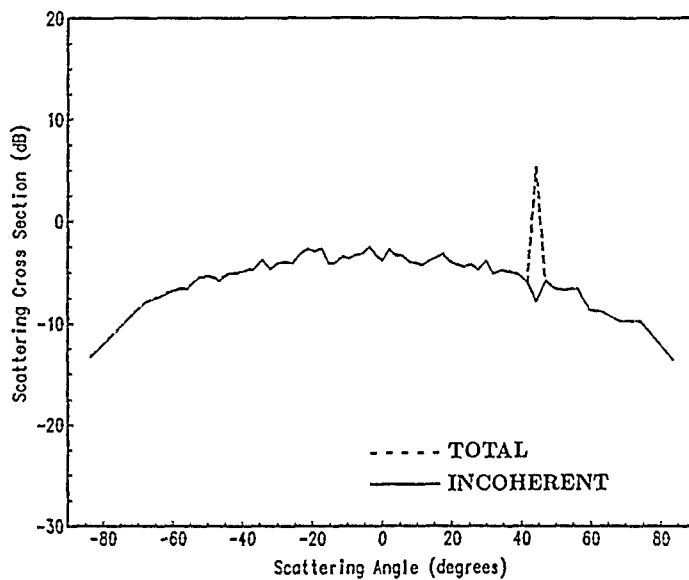


Figure 5.12: Incoherent and Total Scattering Cross Sections: ($\theta_i = 44.06^\circ$, $h/\lambda = 0.141$, $l/\lambda = 0.40$, $L/\lambda = 30.20$)

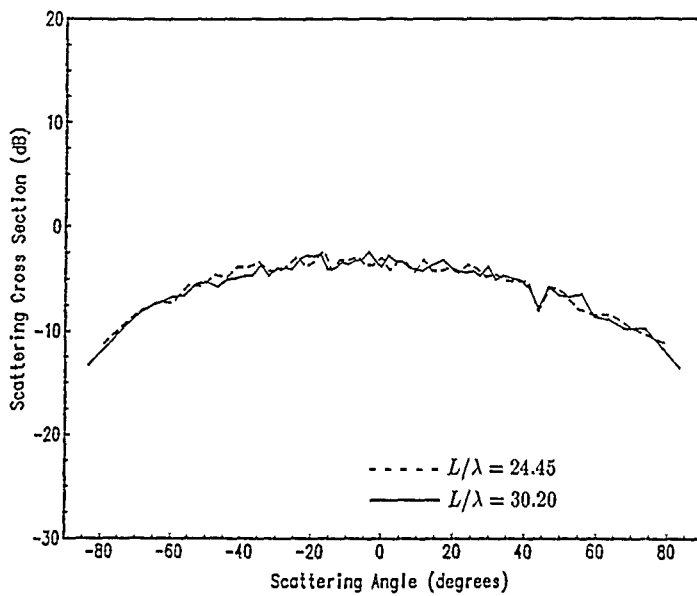


Figure 5.13: Comparison of FEM for $L/\lambda = 30.20$ and $L/\lambda = 24.45$: ($h/\lambda = 0.141$, $l/\lambda = 0.40$)

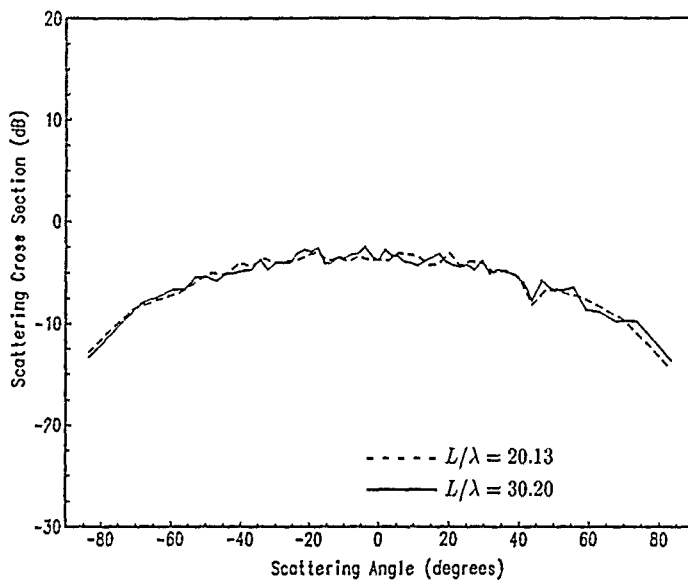


Figure 5.14: Comparison of FEM for $L/\lambda = 30.20$ and $L/\lambda = 20.13$: ($h/\lambda = 0.141$, $l/\lambda = 0.40$)

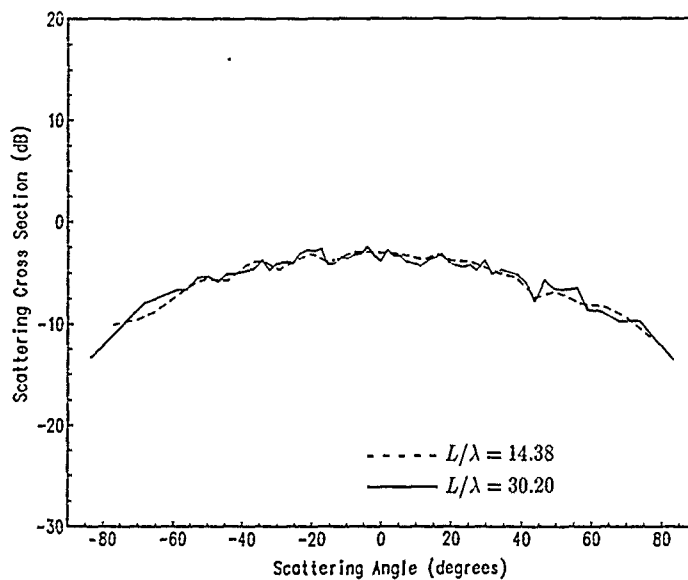


Figure 5.15: Comparison of FEM for $L/\lambda = 30.20$ and $L/\lambda = 14.38$: ($h/\lambda = 0.141$, $l/\lambda = 0.40$)

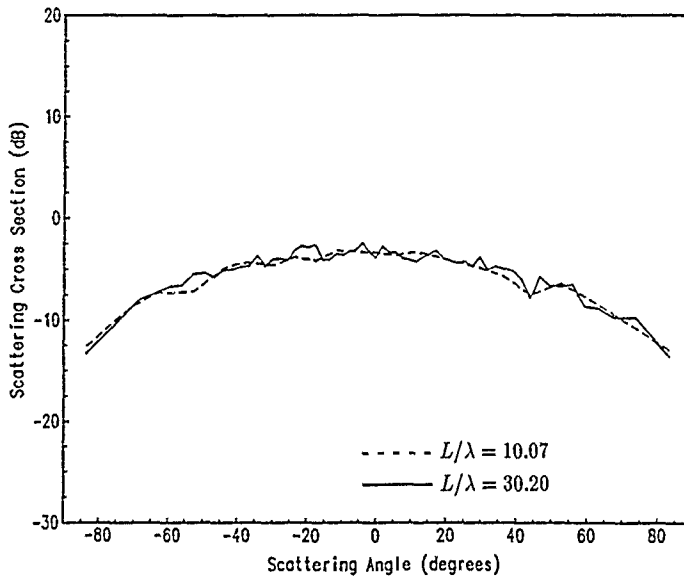


Figure 5.16: Comparison of FEM for $L/\lambda = 30.20$ and $L/\lambda = 10.07$: ($h/\lambda = 0.141$, $l/\lambda = 0.40$)

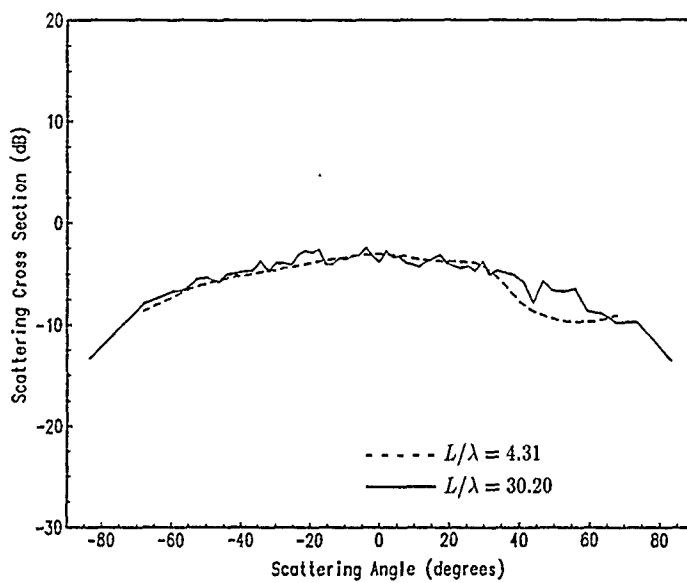


Figure 5.17: Comparison of FEM for $L/\lambda = 30.20$ and $L/\lambda = 4.31$: ($h/\lambda = 0.141$, $l/\lambda = 0.40$)

Chapter 6

CONCLUSIONS

The finite element method is applied to rough surface scattering with periodic, Neumann boundary conditions. Convergence of the result is verified by varying the number of nodes in both the x and z directions. Accuracy is proven through comparison with "exact" results of an integral equation solution and by power conservation tests. Comparisons with the Rayleigh-Rice small perturbation theory and Kirchoff approximations are also made in their respective regions of validity. Finite element advantages over the integral equation approach in both computer CPU time and required memory storage are demonstrated.

Additional tests show that the surface length necessary for accurate incoherent scattering cross section for the finite element solution is as little as 10.07λ . As a result, substantial savings in required memory storage and CPU time are realized. Additional research is needed in order to explain the resulting depression in the incoherent scattering cross section at $\theta_m = \theta_i$. The depression which existed after removal of the specular peak is unexpected and is not explained by scattering theory. However, results obtained are significant as they make it likely that the finite element method will prove to be a feasible approach to large-scale scattering problems including two-dimensional surface scattering.

BIBLIOGRAPHY

- [1] Axline, R.M. and A.K. Fung, "Numerical Computation of Scattering from a Perfectly Conducting Random Surface," *IEEE Transactions on Antennas and Propagation*, Vol AP-26, No. 3, pp. 482-488, 1978.
- [2] Beckmann, P. and Andre Spizzichino, *The Scattering of Electromagnetic Waves from Rough Surfaces*, The Macmillan Company, New York, 1963.
- [3] Chen, J.S. and A. Ishimaru, "Numerical Simulation of the Second-Order Kirchhoff Approximation for Very Rough Surfaces and a Study of Backscattering Enhancement," *J. Acoust. Soc. Am.*, in press 1990.
- [4] Chen, J.S., "Wave Scattering from Very Rough Surfaces and a Study of Backscattering Enhancement," Ph.D. Dissertation, Univ. of Wash., Seattle, 1990.
- [5] Fung, A.K. and M.F. Chen, "Numerical Simulation of Scattering from Simple and Composite Random Surfaces," *J. Opt. Soc. Am.*, Vol. 2, No. 12, pp. 2274-2284, 1985.
- [6] Ishimaru, A., *Wave Propagation and Scattering in Random Media*, Vol I and II, Academic Press, New York, 1978.
- [7] Ishimaru, A., *Electromagnetic Wave Propagation, Radiation, and Scattering*, Prentice Hall, Englewood Cliffs, to be published in January 1991.
- [8] Lou, S.H., L. Tsang, C.H. Chan and A. Ishimaru, "Monte Carlo Simulations of Scattering of Waves by a Random Rough Surface with the Finite Element Method and the Finite Difference Method," *Microwave and Optical Technology Letters*, Vol 3, No. 5, pp. 150-154, 1990.

- [9] Lou, S.H., L. Tsang, C.H. Chan and A. Ishimaru, "Application of Finite Element Method to Monte Carlo Simulations of Scattering of Waves by Random Rough Surfaces with Periodic Boundary Conditions," *Journal of Electromagnetic Waves and Applications*, in press 1990.
- [10] Nieto-Vesperinas and J.M. Soto-Crespo, "Monte Carlo Simulations for Scattering of Electromagnetic Waves from Perfectly Conductive Random Rough Surfaces," *Optics Letters*, Vol 12, No. 12, pp. 979-981.
- [11] Ratnajeevan, S. and H. Hoole, *Computer-Aided Analysis and Design of Electromagnetic Devices*, Elsevier, New York, 1989.
- [12] Sabonnadiere, J.C. and Jean-Louis Coulomb, *Finite Element Methods in CAD: Electrical and Magnetic Fields*, Springer-Verlag New York Inc., New York, 1987.
- [13] Shen, J. and A.A. Maradudin, "Multiple Scattering of Waves From Random Rough Surfaces," *Phys. Rev. B*, Vol 22, pp. 4234-4240, 1980.
- [14] Silvester, P.P. and R.L. Ferrari, *Finite Elements for Electrical Engineers*, Cambridge University Press, New York, 1990.
- [15] Thomas, T.R., *Rough Surfaces*, Longman, New York, 1982.
- [16] Thorsos, Eric I. and Darrell R. Jackson, "The Validity of the Kirchhoff Approximation for Rough Surface Scattering Using a Gaussian Roughness Spectrum," *J. Acoust. Soc. Am.*, Vol. 83, No. 1, pp. 78-92, 1988.
- [17] Thorsos, Eric I. and Darrell R. Jackson, "The Validity of the Perturbation Approximation for Rough Surface Scattering Using a Gaussian Roughness Spectrum," *J. Acoust. Soc. Am.*, Vol. 86, No. 1, pp. 211-277, 1989.
- [18] Zienkiewicz, O.C., *The Finite Element Method*, Third Edition, McGraw Hill, New York, 1977.